University of Groningen

Resolving hydrogen atoms at metal-metal hydride interfaces

de Graaf, Sytze; Momand, Jamo; Mitterbauer, Christoph; Lazar, Sorin; Kooi, Bart J.

IMPORTANT NOTE: You are advised to consult the publisher's version (publisher's PDF) if you wish to cite from it. Please check the document version below.

Document Version
Publisher's PDF, also known as Version of record

Link to publication in University of Groningen/UMCG research database

MATERIALS SCIENCE

Resolving hydrogen atoms at metal-metal hydride interfaces

Sytze de Graaf[1]*, Jamo Momand[1], Christoph Mitterbauer[2], Sorin Lazar[2], Bart J. Kooi[1]*

Hydrogen as a fuel can be stored safely with high volumetric density in metals. It can, however, also be detrimental to metals, causing embrittlement. Understanding fundamental behavior of hydrogen at the atomic scale is key to improve the properties of metal-metal hydride systems. However, currently, there is no robust technique capable of visualizing hydrogen atoms. Here, we demonstrate that hydrogen atoms can be imaged unprecedentedly with integrated differential phase contrast, a recently developed technique performed in a scanning transmission electron microscope. Images of the titanium-titanium monohydride interface reveal stability of the hydride phase, originating from the interplay between compressive stress and interfacial coherence. We also uncovered, 30 years after three models were proposed, which one describes the position of hydrogen atoms with respect to the interface. Our work enables previously unidentified research on hydrides and is extendable to all materials containing light and heavy elements, including oxides, nitrides, carbides, and borides.

INTRODUCTION

Hydrogen is the most abundant but also the most lightweight element in the universe. Therefore, its direct imaging with atomic-scale spatial resolution has, to date, remained elusive, despite the important role hydrogen plays in various fields such as hydrogen storage (*1, 2*) and hydrogen embrittlement (*3–5*). Nowadays, the atomic structure of most crystals can be resolved by imaging techniques based on transmission electron microscopy (TEM) and scanning TEM (STEM), which have reached resolutions well below 100 pm, after the introduction of powerful field-emission electron sources and aberration correctors (*6–8*). However, the challenge of imaging hydrogen has remained, not only because of its low weight but also particularly due to the weight difference between hydrogen and the host atoms in the crystal. Consequently, hydrogen has not been imaged before at an interface with vastly different concentrations of hydrogen on both sides of the interface, despite this being most interesting from a materials science perspective.

In an aberration-corrected STEM, the electrons are accelerated and focused into a subangstrom-sized probe that scans across the surface of a thin specimen (Fig. 1A). The incident electrons interact with the specimen's local electrostatic fields as they propagate through the material and produce a scattered exit beam of electrons that form a diffraction pattern in the detector plane. The detectors collect the electrons from a part of the diffraction pattern, of which the integrated intensity is related to the material's electrostatic field at the probe position.

The popular high-angle annular dark-field (HAADF) STEM technique collects the electrons scattered to high angles using an annular detector. This technique is not affected by the wave character of the electrons that gives interferences, complicating the interpretation of images. Consequently, HAADF-STEM images are readily interpretable, as atomic columns in a crystal are always imaged as bright dots in a dark surrounding with a dot brightness scaling with the average atomic number Z in the atomic column (typically $Z^{1.6-2.0}$)

(*9, 10*). Using this technique, even single carbon atoms can be detected in graphene (*11–13*), and boron and nitrogen can be distinguished in 2D-BN (*14*). However, materials often consist of elements with a large difference in atomic number, such as heavy metal atoms next to light atoms like oxygen, nitrogen, carbon, or hydrogen, where the scattering strength of the light elements compared with the heavy element is too low to be detected. Therefore, it is not possible to image light and heavy elements simultaneously with HAADF-STEM.

In annular bright-field (ABF) STEM, the collection angles are reduced drastically to get sufficient signal from light elements. Nowadays, light elements such as oxygen, nitrogen, and lithium can be imaged routinely with ABF-STEM (*15–17*). In the past decade, this also led to the breakthrough of imaging hydrogen in bulk crystals of YH_2 (*18*), VH_2 (*19*), and NbH_2 (*20*). However, this is only possible under special circumstances, because the specimens must be very thin, i.e., less than 10 nm; otherwise, the signal from the hydrogen atoms cannot be detected. Unfortunately, not all materials can be thinned down to this level, due to limitations such as preparation-induced damage layers, surface oxides, or sample stability. In addition, the ABF-STEM technique automatically reintroduces the wave interference effects in the imaging, which can cause atom columns to appear white or black and generate image artefacts, making unambiguous detection of the light element challenging. Consequently, ABF-STEM cannot robustly image hydrogen atoms in realistic material systems, i.e., those that are thick and distorted, and has, therefore, been limited to model materials.

Here, we image hydrogen atoms at a metal-metal hydride interface with the recently developed integrated differential phase contrast (iDPC) technique. With this technique, coherently scattered electrons that fall inside the bright-field disk are collected with an annular detector that is segmented into four quadrants (Fig. 1A) (*21*). Using DPC imaging (*22–24*), three complementary images are formed that represent the material's local projected electrostatic properties when the specimen is thin. Then, the projected electric field is imaged with DPC, the projected charge density with differentiated DPC (dDPC), and the projected potential with iDPC (see also the Supplementary Materials) (*21*). The iDPC technique is particularly useful to generate sensitivity toward light elements (*25, 26*). However, the direct relation

[1]Zernike Institute for Advanced Materials, University of Groningen, Nijenborgh 4, 9747 AG Groningen, Netherlands. [2]Thermo Fisher Scientific, Achtseweg Noord 5, 5651 GG Eindhoven, Netherlands.
*Corresponding author. Email: sytze.de.graaf@rug.nl (S.d.G.); b.j.kooi@rug.nl (B.J.K.)
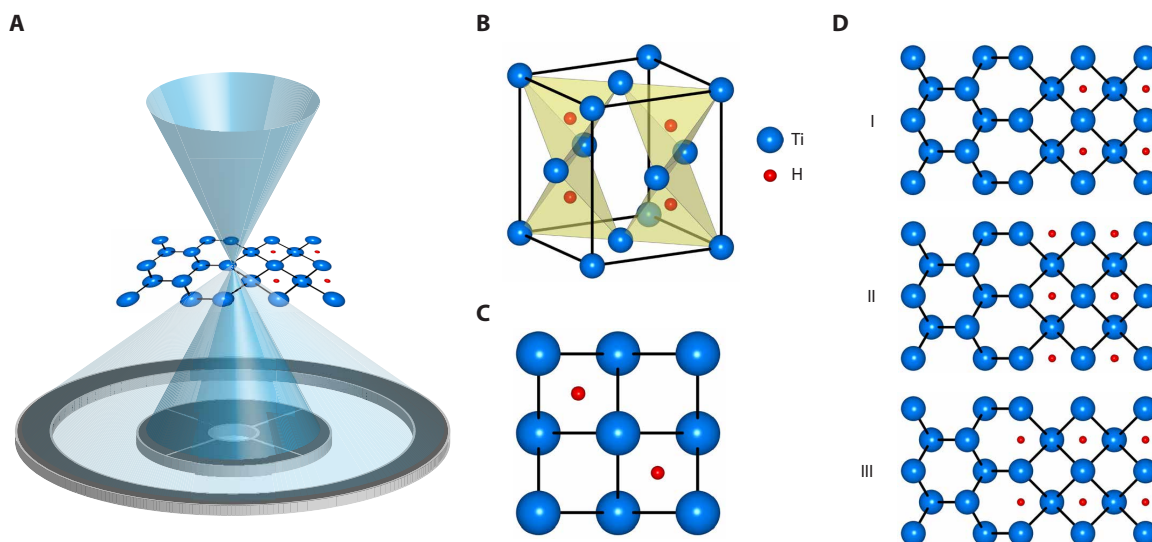
Fig. 1. Schematic of a STEM system and the γ-TiH crystal and its three possible interfaces with α-Ti. (**A**) iDPC images are captured with the quadrant detector (inner) and can be used simultaneously with the HAADF detector (outer). (**B**) Crystal structure model of the face-centered tetragonal (FCT) γ-TiH unit cell containing four hydrogen atoms that occupy tetrahedral sites. (**C**) Two columns in between the titanium columns are occupied by hydrogen atoms and two columns are empty. (**D**) Three potential models can describe the interface between γ-TiH and α-Ti.

between iDPC and the material's electrostatic properties only holds in cases where the specimen is ultrathin. Usually, the specimens are thicker, and the physical interpretation of the DPC images becomes less straightforward. Nevertheless, advantages of iDPC over ABF are (i) the capability to directly image the projected potential for thin specimens, (ii) a simpler contrast transfer function, i.e., less problems with the wave interference character and contrast reversals in the images, and (iii) an intrinsically better signal-to-noise ratio (SNR), which in the end also provides the option to use lower doses, e.g., on vulnerable samples such as the beam-sensitive zeolite (*27*).

RESULTS

To produce stable metal-metal hydride interfaces, we have chosen the Ti-TiH system, which is similar to the Zr-ZrH system that plays an important role as nuclear fuel cladding material in nuclear reactors (*28*). In contrast to earlier studies that image hydrogen in a dihydride like YH_2, here we study the monohydride γ-TiH. This hydride readily forms at low temperature and low hydrogen concentrations due to the high hydrogen mobility and low room temperature hydrogen solubility limit in hexagonal close-packed α-Ti (*29*, *30*). The structure of this phase has been identified by diffraction techniques already more than three decades ago (*29–31*). The γ-TiH crystal has a face-centered tetragonal (FCT) lattice that contains four titanium and four hydrogen atoms per unit cell (Fig. 1B). Half of the tetrahedral interstitial sites are occupied by hydrogen atoms that organize in two columns that are parallel to the *c* axis and are located on the face diagonal when viewed along the *c* axis (Fig. 1C). Ab initio calculations performed on the isomorphic γ-ZrH indicate that, despite a lower entropy contribution, this ordering of hydrogen in columns is more stable than the diamond-like occupation, where the hydrogen atoms occupy alternating tetrahedral sites (*32*). A similar result, although described less explicitly, was obtained for γ-TiH (*33*).

Imaging the monohydride offers major benefits over a dihydride because in single images, we can image columns with identical surrounding of the host Ti atom columns where one type of column contains the hydrogen atoms and the other type, in principle, is empty. Wave interference effects of the scanning electron beam play a role during imaging; therefore, it cannot be ruled out that there is a certain atomic like signal in a column between Ti atom columns when no hydrogen atoms are present. In the monohydride, the difference between the signals coming from the hydrogen-filled columns and the empty columns can be directly compared, allowing for unambiguous interpretation that is not possible in the case of the dihydride. Imaging artefacts are often a challenge: In TEM and STEM, such artefacts generally have a symmetry related to the one of the underlying host lattices. In this respect, the monohydride offers a further advantage because the symmetry of the hydrogen sublattice is distinctly different from the one of the host titanium sublattice, and therefore, the weak signals we measure for the hydrogen cannot be a faint displaced or distorted replica of the host.

Although γ-TiH has an approximately 15% larger unit cell volume compared with the α-Ti matrix, an apparently strain-free coherent interface is formed between them (*34*). Therefore, to accommodate the volume misfit, the lattice misfit perpendicular to the interface is about 16%, generating large compressive stress on the precipitate (*31*). Consequently, the growth rate parallel to the interface is orders of magnitude higher than the perpendicular one, resulting in plate-shaped precipitates (*31*, *34*). The absolute position of the hydrogen atoms with respect to the interface has to date not yet been identified, because diffraction techniques do not transfer translational information and real-space atomic resolution images only provided information on the position of the titanium columns (*34*). Hence, there are three possible models, schematically depicted in Fig. 1D, which could not be distinguished using earlier techniques (*34*).

To image the interface edge-on, we align the α-Ti matrix along the [0001] direction, and then the FCT γ-TiH is imaged along [001]. However, the large volume expansion by the incorporation of the γ-TiH precipitate in the Ti matrix leads to a severely strained system, where the misfit is accommodated plastically via dislocation motion in

the Ti matrix (*31, 35*). Consequently, an often encountered challenge, particularly when thinning the sample to electron transparency, is that crystal bending across the interface misaligns the crystal locally and impedes proper atomically resolved images over the entire region of interest (fig. S4). Because of these random imperfections in the crystal, it is essential to capture high-resolution images of large areas as fast as possible to locally obtain the highest possible quality of atomically resolved images while minimizing drift. In this context, the detectors that we use here have an advantage over pixelated detectors that were used in recent demonstrations of ptychographic reconstruction (*36–38*). The pixelated detector captures a complete diffraction pattern at every scan position, yielding a large four-dimensional dataset. With this abundant dataset, the local phase change can be retrieved for ultrathin specimens using an iterative phase retrieval algorithm. However, currently, a serious drawback of a pixelated detector is the two-orders-of-magnitude-longer pixel dwell time (*36*) compared with the HAADF, ABF, and quadrant DPC detectors. Hence, despite not being a model system for imaging due to strain, bending, and large sample thickness (see the Supplementary Materials), we were able to find well-aligned areas at the interface by capturing large areas with small pixel size and quick readout times of several seconds. With this approach, we routinely imaged the edge-on interface with minimal residual misalignment with about 60-pm resolution (Fig. 2).

The image recorded with the HAADF detector can be interpreted directly by virtue of Z-contrast: It shows two distinguishable lattices separated by an atomically sharp interface that matches convincingly with the simulated image (Fig. 2A). Viewed along these crystal axes,

the α-Ti(01$\bar{1}$0) planes are parallel to the γ-TiH(1$\bar{1}$0) planes at the interface, in agreement with the TEM studies that were performed over three decades ago (*31, 34*). Although the Z-contrast image visualizes the titanium atoms well, it fails to transfer signal from the hydrogen atoms, which are expected in equivalent stoichiometry in the γ-TiH.

Next, we used ABF to image the α-Ti/γ-TiH interface (Fig. 2B), although the specimen thickness of about 30 nm is substantially thicker than 10 nm, which is required to properly image hydrogen atoms with ABF. The titanium atoms are well resolved in the γ-TiH but poorly in the α-Ti. The high sensitivity of ABF imaging toward crystal orientation (see fig. S11) combined with the inherent local bending of the specimen leads to the lower quality of the ABF image compared with the HAADF image (*16*). Nonetheless, in the γ-TiH, a weak contrast is visible between alternating atomic planes parallel and perpendicular to the interface, which indicates the presence of signal from the hydrogen columns. Close inspection suggests that either model I or III best describes the interface (Fig. 1D). However, being limited by the SNR and quality of the image, we cannot reliably determine the exact position of hydrogen columns.

As a final step, the DPC-based images of the interface were constructed using the segmented detector and are depicted in Fig. 2 (C to F). In the iDPC image, the Ti atoms are resolved accurately in the γ-TiH and the α-Ti matrix (Fig. 2C). Besides the bright Ti atoms, there is also a clear signal within the γ-TiH crystal that forms a checkerboard-like pattern with the symmetry that is expected for the hydrogen sublattice. With the convincing match between the experimental and simulated images and the extensive additional
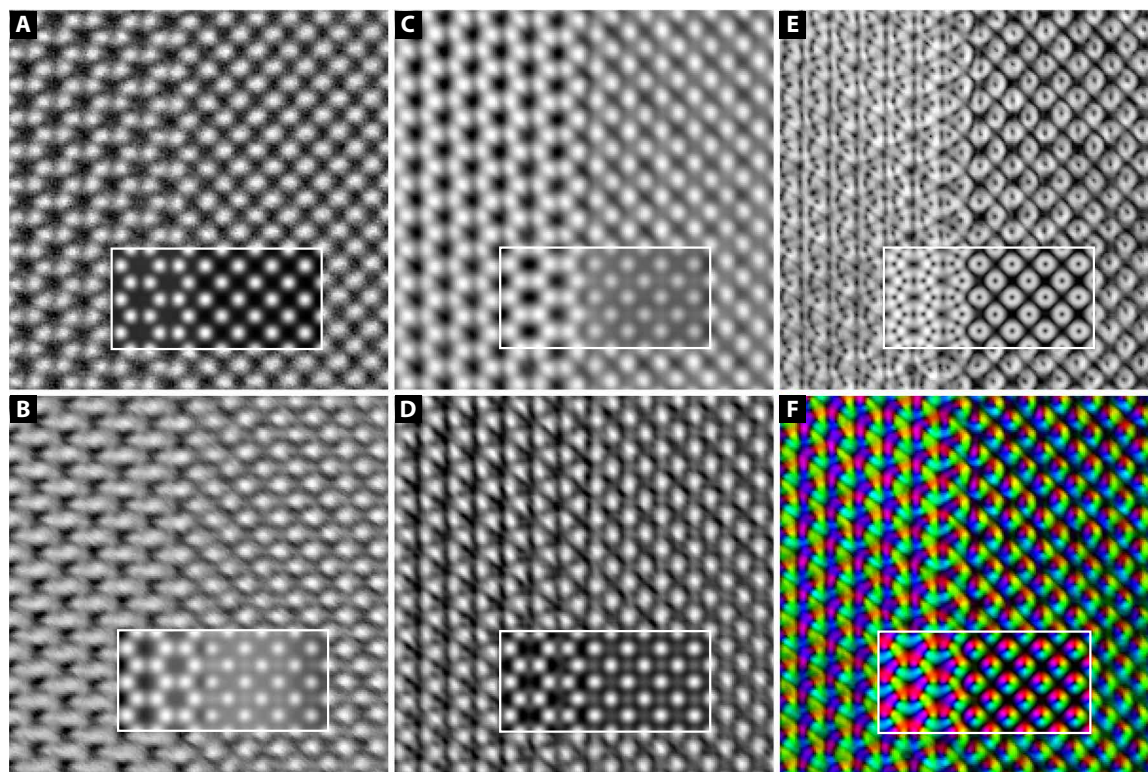

Fig. 2. Comparison of images of the interface between γ-TiH and α-Ti using different techniques. (**A**) HAADF. (**B**) Contrast-inverted ABF. (**C**) iDPC. (**D**) Contrast-inverted dDPC. (**E**) DPC magnitude. (**F**) DPC vector field using color wheel representation. Insets: Simulated images of a 30-nm-thick specimen of interface model I shown in Fig. 1D. Field of view is 3.5 × 3.5 nm.

checks that we have performed (see the Supplementary Materials, e.g., providing different types of electron energy loss spectroscopy information and results of extensive image simulations), we show that the hydrogen columns are imaged with iDPC and that the interface is best described by model I (Fig. 1D).

In the dDPC image (Fig. 2D), the Ti atoms are properly resolved throughout the entire image, in contrast to the ABF image where they were only well resolved in the γ-TiH. Also, the hydrogen atom columns are imaged, but, as in the ABF image, the faint signal is preventing accurate hydrogen column detection in the image. The DPC images in Fig. 2 (E and F) show the scalar field magnitude and the vector field, where the field direction is indicated by the color and the magnitude by the intensity. Figure 2E displays a rather complex field in the Ti matrix and a more easily interpretable field in the γ-TiH, which agrees well with the simulation. The field magnitude at the Ti atom columns in the γ-TiH is not radially symmetric, but is ellipse shaped and oriented in two orthogonal directions. This is a direct effect of the checkerboard-like ordered hydrogen columns and also allows us to confirm model I as the best description of the interface.

We have performed an SNR analysis of the hydrogen signal as a measure to quantify the hydrogen imaging capabilities of the different imaging techniques (Fig. 3). Note that we have applied an identical filtering procedure to all experimental images to ensure a fair comparison (see fig. S6). Experimental intensity profiles are extracted by averaging the alternating (220) atomic planes (perpendicular to the interface) containing hydrogen columns (Ti-H-Ti) and the intermediate planes containing empty columns (Ti-empty-Ti). These are compared with the simulated intensity profiles of a 32.2-nm-thick specimen (see Fig. 3), but note that the iDPC images compare reasonably well with simulations holding for a large thickness range of 20 to 50 nm (fig. S13). We define the SNR as the ratio of the relative intensity of the hydrogen signal and the SD of the averaged intensity profiles.

The HAADF intensity profiles only contain peaks from Ti and no signal from hydrogen; hence, as expected, the SNR is below unity (Fig. 3A). In the ABF image, the hydrogen atom columns are imaged with an SNR of 2–3 (Fig. 3B). However, also an image artefact is

revealed: The intensity of the adjacent Ti atom columns is modulated with the symmetry of the checkerboard-like ordered hydrogen atoms. The SNR is also 2–3 in the dDPC image, where the hydrogen atoms produce the sharpest peak (Fig. 3C). However, at the same time, peaks are present in the empty columns, which complicate image interpretation. Last, the intensity profiles from the iDPC image show that hydrogen atoms are imaged with the highest SNR of 4–5, and no image artefacts are present (Fig. 3D). The SNR of the iDPC image compared with that of the ABF image is improved, because on the one hand, the segmented detector collects more electrons, while on the other hand, the random noise is suppressed by its intrinsic noise suppression property (21, 27). Furthermore, the inherently present specimen bending reduces signal from the hydrogen columns for ABF and substantially less for iDPC (see figs. S7 and S11).

We did not observe any structural rearrangements of hydrogen atoms at the interface during the imaging, i.e., we were limited by carbon contamination and not by electron beam–induced damage. This is a remarkable observation, considering that (i) energetic electrons are impinging on the specimen during imaging, which can either transfer energy to the material or displace hydrogen or titanium atoms upon knock-on collisions (39), (ii) hydrogen atoms are highly mobile in titanium at room temperature, (iii) there is a step function in hydrogen concentration of about 50 atomic percent across the interface, and (iv) the γ-TiH is a metastable phase. Therefore, our observation is at first sight contrary to what is expected based on these considerations. However, energy transferred by inelastic collisions of the 300-keV primary electrons with the atoms can be quickly dissipated because of the metallic behavior of titanium hydrides (40). Knock-on collision of a primary electron with a hydrogen or titanium atom can lead to a maximum energy transfer of 844 and 17.8 eV, respectively. This amount of energy is sufficiently high to displace hydrogen atoms but not titanium atoms, if we assume a typical binding energy of 25 eV (41). Nevertheless, overall, the probability to displace a hydrogen atom may still be low, because the scattering cross section of the hydrogen atom is small and it decreases with increasing primary electron energy (39). Therefore, it is advantageous to image the titanium hydride with higher electron energies (like 300 keV) to minimize electron beam–induced damage. Furthermore, for a complete understanding,
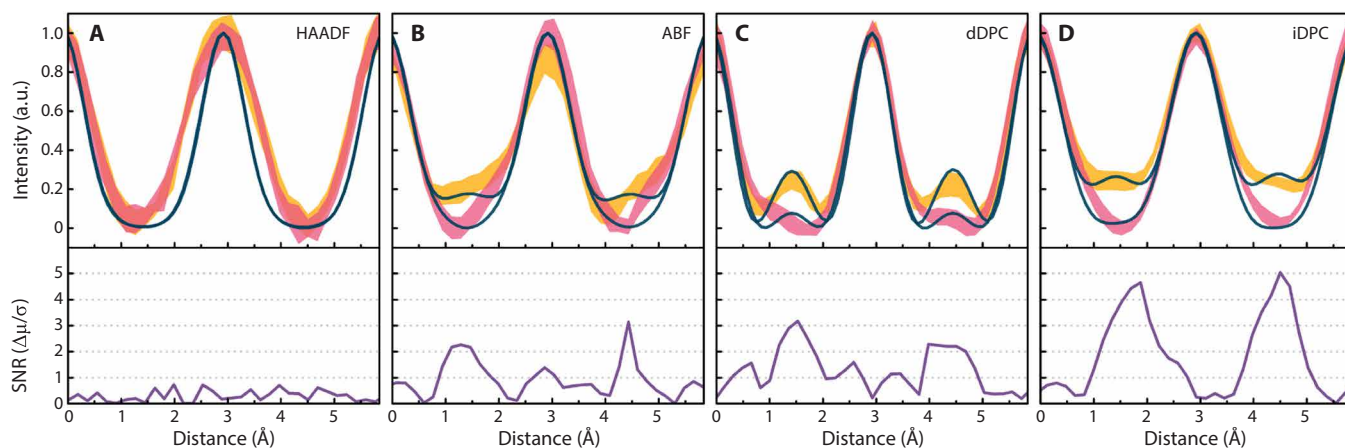
Fig. 3. Comparison of the experimental and simulated intensity profiles of the γ-TiH at the metal–metal hydride interface and the experimental SNR of the hydrogen column signal. (**A**) HAADF. (**B**) ABF. (**C**) dDPC. (**D**) iDPC. The pink and yellow bands represent the experimental intensity profiles of the Ti-empty-Ti-empty-Ti and Ti-H-Ti-H-Ti columns, respectively. The width of the bands is twice the SD, centered around the average value. Solid dark lines are the simulated profiles for a 32.2-nm-thick γ-TiH crystal. The SNR of the hydrogen signal is extracted from the experimental profiles and plotted below. a.u., arbitrary units.

it is also critical to consider the effects of embedding the γ-TiH precipitate in the host metal. Ab initio simulations (*33*) have demonstrated that the γ-TiH precipitate cannot be stabilized by compressive stress imposed by the matrix alone. Only when the combined effect of compressive stress imposed by the matrix, and the coherency strains of the interface are taken into account, the γ-TiH precipitate is stabilized. These arguments rationalize our observation that the Ti/γ-TiH interface remains stable during imaging and that electron beam–induced damage is not visible. We additionally observed that after preparation, the γ-TiH remains only crystalline in reasonably thick (e.g., 30 nm or thicker) parts of the specimen. We speculate that the thinner parts of the specimen are easier amorphized during preparation, as it may not have the mechanical rigidity to provide sufficient coherency strains and compressive stresses that stabilize the γ-TiH. Hence, the dynamic interplay between compressive stress and the formation of a coherent interface is directly responsible for the high stability of the Ti/γ-TiH interface.

Higher-quality images of the γ-TiH are captured further away from the interface where the crystal strain has relieved and local bending is much less a problem (Fig. 4). A result is that the hydrogen columns appear more localized compared with the images that are recorded at the interface. Now, the checkerboard-like filling of the hydrogen columns in the γ-TiH lattice is visible in the ABF (Fig. 4B) and iDPC (Fig. 4C) images, which is lacking in the HAADF-STEM image (Fig. 4A). Here, we constructed the ABF image by summing the four images from the quadrant detector, because with the normal ABF geometry a signal from the hydrogen atoms could not be detected. A similar detector geometry was also used to image hydrogen in VH_2 (*19*). Our simulations show that in this case, a higher hydrogen column intensity can be achieved at the costs of localization (fig. S7). Now, the hydrogen columns are also readily observable next to the titanium ones in the ABF image. Nevertheless, the hydrogen atoms are much better visualized in the iDPC image.

Compared with Fig. 3, the experimental intensity profiles extracted from the images in Fig. 4 now match significantly better with the simulated ones as the crystal is better oriented (see Fig. 5). In particular, the profiles extracted from the HAADF and iDPC images agree nearly perfectly with the simulations. However, the intensity profile from the ABF image does not match well and contains high levels of noise. The noise in the iDPC image is three times lower than that in the ABF image, which is a remarkable result, considering that the ABF and iDPC images are constructed from the exact identical original signal. This demonstrates the intrinsic noise-suppressing property of using in a clever way the four quadrants of the iDPC imaging technique.

DISCUSSION
Our experimental images and extensive image simulations of the γ-TiH unit cell (see the Supplementary Materials) allow us to conclude that iDPC has several major advantageous over ABF imaging: (i) iDPC images the hydrogen columns with higher contrast and better localization. (ii) The atom column intensity oscillates substantially less as a function of specimen thickness. (iii) Contrast also does not reverse as long as the probe is focused into the specimen, unlike ABF imaging where the empty column and hydrogen-filled column reverse contrast for specimens thinner than about 10 nm. This furthermore shows that the iDPC technique produces easily interpretable images also when the specimen is thick. However, then, the iDPC
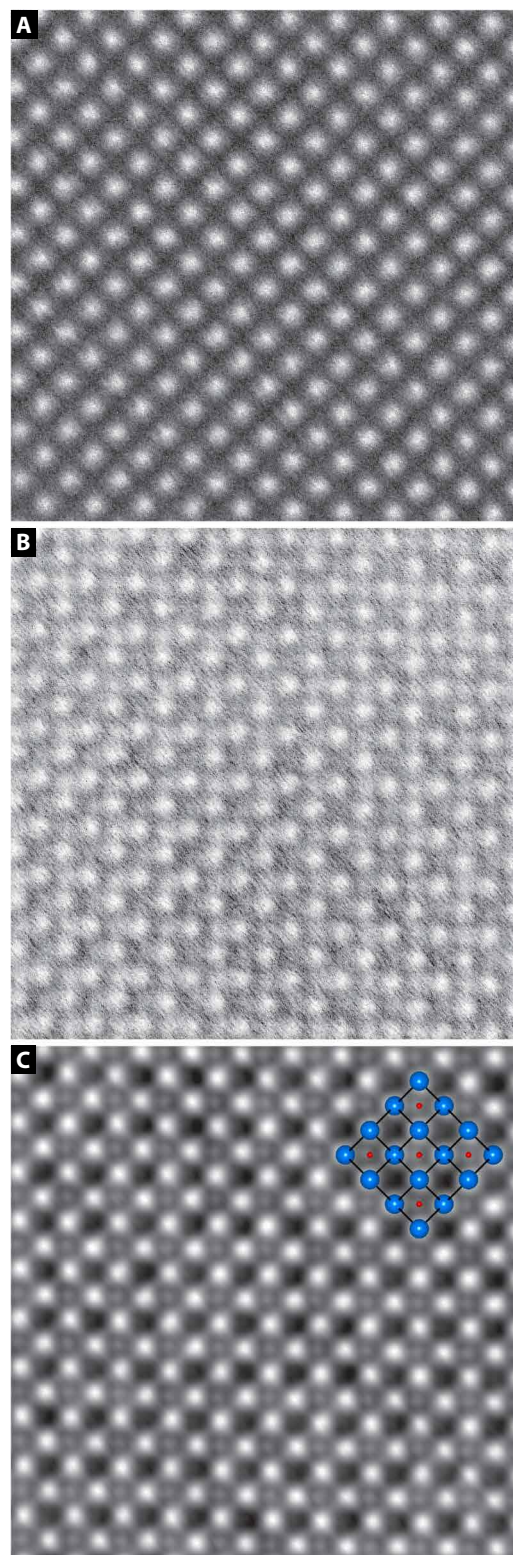
Fig. 4. Comparison of high-quality images of γ-TiH far away from the interface. (**A**) HAADF. (**B**) Contrast-inverted ABF. (**C**) iDPC. Field of view is 3.13 × 3.13 nm.
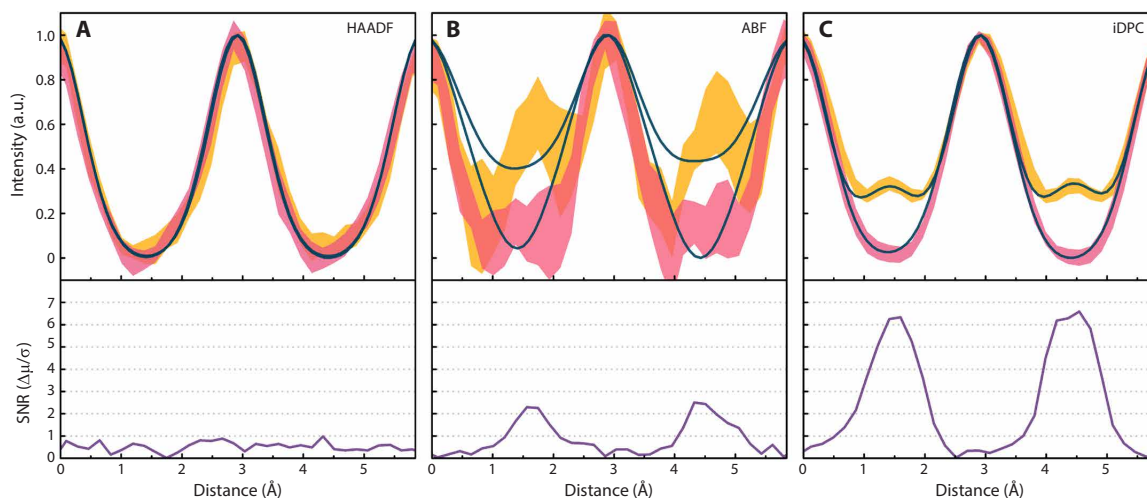
Fig. 5. Comparison of the experimental and simulated intensity profiles of the γ-TiH under optimal imaging conditions and the SNR of the hydrogen column signal. (**A**) HAADF. (**B**) ABF. (**C**) iDPC. Here, the ABF is formed by summing the quadrants of the iDPC detector, such that the ABF and iDPC images use the exact identical raw data. The pink and yellow bands represent the experimental intensity profiles of the Ti-empty-Ti-empty-Ti and Ti-H-Ti-H-Ti columns, respectively. The width of the bands is twice the SD, centered around the average value. Solid dark lines are the simulated profiles for a 52-nm-thick γ-TiH crystal. The SNR of the hydrogen signal is extracted from the experimental profiles and plotted below.

image cannot be quantitatively interpreted as the material's projected potential. This is also evident, since we observe in the experiment and in the simulation that the atom intensities oscillate as a function of thickness and also that the relative contrast of the hydrogen atoms is higher than expected based on the atomic weights of hydrogen and titanium. Nevertheless, these simulation results demonstrate that, on fairly all aspects, iDPC images allow more straightforward interpretation and better imaging of the light element column next to an empty column. In ABF, the signals coming from the hydrogen column and the empty column are very similar and can reverse in contrast, which shows that ABF is prone to erroneous detection of light elements.

In summary, we have imaged hydrogen atoms in titanium monohydride at its interface with titanium using the recently developed iDPC-STEM technique. The images of the interface uncovered, 30 years after three models were proposed, the model that describes the positions of the hydrogen atoms with respect to the interface. We observed unexpected high stability of the titanium monohydride even during energetic electron irradiation conditions, originating from the combined effect of interfacial coherency strains and the compressive stress imposed by the matrix. Significantly, the capabilities of imaging hydrogen in the nonideal titanium-titanium monohydride system, with severe and limiting imperfections, demonstrate the ability and the prospects of iDPC-STEM as a robust imaging tool in materials research. This work paves the way to further advance our understanding of hydrogen in solids, like retrieving local site occupancy, atomic vibrations, and mobility from iDPC images. Moreover, it can be extended to all material systems containing light elements next to heavy ones, like oxides, nitrides, carbides, and borides.

MATERIALS AND METHODS
Specimen preparation
A single crystal titanium sample was mechanically polished followed by twin-jet electrochemical polishing at room temperature with a TenuPol-3 from Struers to load the sample with hydrogen such that

γ-TiH precipitates were formed. A TEM lamella was extracted from the sample using a Helios G4 CX dual beam system with a Ga focused ion beam. The lamella was thinned to electron transparency with the focused ion beam using progressively lower accelerating voltages. As a final step, a Gatan PIPS II polishing system was used to polish the lamella with 0.3-kV Ar ions.

Scanning transmission electron microscopy
For the imaging, we used a probe and image corrected Thermo Fisher Scientific Themis Z S/TEM system operating at 300 kV. The specimen was plasma cleaned for 3 min before insertion in the S/TEM column. For the imaging, a convergence semiangle of 21 mrad was used, and the current was set to 50 pA for Fig. 2 and 14 pA for Fig. 4. Experimental images were identically filtered by applying a high-pass Gaussian filter and an average background subtraction filter.

Multislice simulations
The crystallographic models of the γ-TiH unit cell and the γ-TiH/α-Ti interface were constructed with VESTA. The γ-TiH unit cell was adjusted (<2% change in lattice parameters) to obtain a coherent interface with α-Ti. These models were loaded in the Dr. Probe software for STEM image simulations. Microscope parameters were set equal to experimentally calibrated values, and aberrations were neglected except for defocus. The detector collection angles were also set to the experimentally calibrated values. The resulting images were convolved with a two-dimensional Gaussian function of 70-pm full-width at half maximum to account for finite probe size.

SUPPLEMENTARY MATERIALS
Supplementary material for this article is available at http://advances.sciencemag.org/cgi/content/full/6/5/eaay4312/DC1

REFERENCES AND NOTES

1. L. Schlapbach, A. Züttel, Hydrogen-storage materials for mobile applications. *Nature* **414**, 353–358 (2001).

2. B. Sakintuna, F. Lamari-Darkrim, M. Hirscher, Metal hydride materials for solid hydrogen storage: A review. *Int. J. Hydrog. Energy* **32**, 1121–1140 (2007).

3. J. Song, W. A. Curtin, Atomic mechanism and prediction of hydrogen embrittlement in iron. *Nat. Mater.* **12**, 145–151 (2013).

4. A. Barnoush, H. Vehoff, Recent developments in the study of hydrogen embrittlement: Hydrogen effect on dislocation nucleation. *Acta Mater.* **58**, 5274–5285 (2010).

5. M. S. Daw, M. I. Baskes, Semiempirical, quantum mechanical calculation of hydrogen embrittlement in metals. *Phys. Rev. Lett.* **50**, 1285–1288 (1983).

6. M. Haider, S. Uhlemann, E. Schwan, H. Rose, B. Kabius, K. Urban, Electron microscopy image enhanced. *Nature* **392**, 768–769 (1998).

7. R. Erni, M. D. Rossell, C. Kisielowski, U. Dahmen, Atomic-resolution imaging with a sub-50-pm electron probe. *Phys. Rev. Lett.* **102**, 096101 (2009).

8. H. Sawada, Y. Tanishiro, N. Ohashi, T. Tomita, F. Hosokawa, T. Kaneyama, Y. Kondo, K. Takayanagi, STEM imaging of 47-pm-separated atomic columns by a spherical aberration-corrected electron microscope with a 300-kV cold field emission gun. *J. Electron Microsc.* **58**, 357–361 (2009).

9. B. Rafferty, D. Nellist, J. Pennycook, On the origin of transverse incoherence in Z-contrast STEM. *J. Electron Microsc.* **50**, 227–233 (2001).

10. Z. W. Wang, Z. Y. Li, S. J. Park, A. Abdela, D. Tang, R. E. Palmer, Quantitative Z-contrast imaging in the scanning transmission electron microscope with size-selected clusters. *Phys. Rev. B* **84**, 073408 (2011).

11. R. Zan, U. Bangert, Q. Ramasse, K. S. Novoselov, Metal–graphene interaction studied via atomic resolution scanning transmission electron microscopy. *Nano Lett.* **11**, 1087–1092 (2011).

12. H. Sawada, T. Sasaki, F. Hosokawa, K. Suenaga, Atomic-resolution STEM imaging of graphene at low voltage of 30 kV with resolution enhancement by using large convergence angle. *Phys. Rev. Lett.* **114**, 166102 (2015).

13. B. Chen, V. L. Do, G. ten Brink, G. Palasantzas, P. Rudolf, B. J. Kooi, Dynamics of GeSbTe phase-change nanoparticles deposited on graphene. *Nanotechnology* **29**, 505706 (2018).

14. O. L. Krivanek, M. F. Chisholm, V. Nicolosi, T. J. Pennycook, G. J. Corbin, N. Dellby, M. F. Murfitt, C. S. Own, Z. S. Szilagyi, M. P. Oxley, S. T. Pantelides, S. J. Pennycook, Atom-by-atom structural and chemical analysis by annular dark-field electron microscopy. *Nature* **464**, 571–574 (2010).

15. S. D. Findlay, N. Shibata, H. Sawada, E. Okunishi, Y. Kondo, T. Yamamoto, Y. Ikuhara, Robust atomic resolution imaging of light elements using scanning transmission electron microscopy. *Appl. Phys. Lett.* **95**, 191913 (2009).

16. S. D. Findlay, N. Shibata, H. Sawada, E. Okunishi, Y. Kondo, Y. Ikuhara, Dynamics of annular bright field imaging in scanning transmission electron microscopy. *Ultramicroscopy* **110**, 903–923 (2010).

17. Y. Oshima, H. Sawada, F. Hosokawa, E. Okunishi, T. Kaneyama, Y. Kondo, S. Niitaka, H. Takagi, Y. Tanishiro, K. Takayanagi, Direct imaging of lithium atoms in LiV$_2$O$_4$ by spherical aberration-corrected electron microscopy. *J. Electron Microsc.* **59**, 457–461 (2010).

18. R. Ishikawa, E. Okunishi, H. Sawada, Y. Kondo, F. Hosokawa, E. Abe, Direct imaging of hydrogen-atom columns in a crystal by annular bright-field electron microscopy. *Nat. Mater.* **10**, 278–281 (2011).

19. S. D. Findlay, T. Saito, N. Shibata, Y. Sato, J. Matsuda, K. Asano, E. Akiba, T. Hirayama, Y. Ikuhara, Direct imaging of hydrogen within a crystalline environment. *Appl. Phys. Express* **3**, 116603 (2010).

20. Y.-J. Kim, R. Tao, R. F. Klie, D. N. Seidman, Direct atomic-scale imaging of hydrogen and oxygen interstitials in pure niobium using atom-probe tomography and aberration-corrected scanning transmission electron microscopy. *ACS Nano* **7**, 732–739 (2013).

21. I. Lazić, E. G. T. Bosch, S. Lazar, Phase contrast STEM for thin samples: Integrated differential phase contrast. *Ultramicroscopy* **160**, 265–280 (2016).

22. N. H. Dekkers, H. de Lang, Differential phase contrast in a STEM. *Optik* **41**, 452–456 (1974).

23. N. Shibata, S. D. Findlay, Y. Kohno, H. Sawada, Y. Kondo, Y. Ikuhara, Differential phase-contrast microscopy at atomic resolution. *Nat. Phys.* **8**, 611–615 (2012).

24. R. Close, Z. Chen, N. Shibata, S. D. Findlay, Towards quantitative, atomic-resolution reconstruction of the electrostatic potential via differential phase contrast using electrons. *Ultramicroscopy* **159**, 124–137 (2015).

25. E. Yücelen, I. Lazić, E. G. T. Bosch, Phase contrast scanning transmission electron microscopy imaging of light and heavy atoms at the limit of contrast and resolution. *Sci. Rep.* **8**, 2676 (2018).

26. N. Gauquelin, K. H. W. van den Bos, A. Béché, F. F. Krause, I. Lobato, S. Lazar, A. Rosenauer, S. Van Aert, J. Verbeeck, Determining oxygen relaxations at an interface: A comparative study between transmission electron microscopy techniques. *Ultramicroscopy* **181**, 178–190 (2017).

27. I. Lazić, E. G. T. Bosch, Analytical review of direct stem imaging techniques for thin samples, in *Advances in Imaging and Electron Physics*, P. W. Hawkes, Ed. (Elsevier, 2017), vol. 199, pp. 75–184.

28. G. J. C. Carpenter, The precipitation of γ-zirconium hydride in zirconium. *Acta Metall.* **26**, 1225–1235 (1978).

29. O. T. Woo, G. C. Weatherly, C. E. Coleman, R. W. Gilbert, The precipitation of γ-deuterides (hydrides) in titanium. *Acta Metall.* **33**, 1897–1906 (1985).

30. O. T. Woo, J. G. C. Carpenter, γ-TiH: An isomorph of γ-ZrH. *Scr. Metall.* **19**, 931–934 (1985).

31. H. Numakura, M. Koiwa, Hydride precipitation in titanium. *Acta Metall.* **32**, 1799–1807 (1984).

32. C. Domain, R. Besson, A. Legris, Atomic-scale ab-initio study of the Zr-H system: I. Bulk properties. *Acta Mater.* **50**, 3513–3526 (2002).

33. Q. Xu, A. van der Ven, First-principles investigation of metal-hydride phase stability: The Ti-H system. *Phys. Rev. B* **76**, 064207 (2007).

34. A. Bourret, A. Lasalmonie, S. Naka, In-situ high resolution observation of hydride precipitation in titanium. *Scr. Metall.* **20**, 861–866 (1986).

35. D. S. Shih, I. M. Robertson, H. K. Birnbaum, Hydrogen embrittlement of α titanium: In situ tem studies. *Acta Metall.* **36**, 111–124 (1988).

36. Y. Jiang, Z. Chen, Y. Han, P. Deb, H. Gao, S. Xie, P. Purohit, M. W. Tate, J. Park, S. M. Gruner, V. Elser, D. A. Muller, Electron ptychography of 2D materials to deep sub-ångström resolution. *Nature* **559**, 343–349 (2018).

37. H. Yang, R. N. Rutte, L. Jones, M. Simson, R. Sagawa, H. Ryll, M. Huth, T. J. Pennycook, M. L. H. Green, H. Soltau, Y. Kondo, B. G. Davis, P. D. Nellist, Simultaneous atomic-resolution electron ptychography and Z-contrast imaging of light and heavy elements in complex nanostructures. *Nat. Commun.* **7**, 12532 (2016).

38. J. M. Rodenburg, Ptychography and related diffractive imaging methods, in *Advances in Imaging and Electron Physics*, P. W. Hawkes, Ed. (Elsevier, 2008), vol. 150, pp. 87–184.

39. Y. Wang, T. Wakasugi, S. Isobe, N. Hashimoto, S. Ohnuki, Interaction of electrons with light metal hydrides in the transmission electron microscope. *Microscopy* **63**, 437–447 (2014).

40. P. A. T. Olsson, J. Blomqvist, C. Bjerkén, A. R. Massih, *Ab initio* thermodynamics investigation of titanium hydrides. *Comput. Mater. Sci.* **97**, 263–275 (2015).

41. D. B. Williams, B. C. Carter, *Transmission Electron Microscopy - A Textbook for Materials Science* (Plenum Press, New York, 1996).

42. L. Yan, S. Ramamurthy, J. J. Noël, D. W. Shoesmith, Hydrogen absorption into alpha titanium in acidic solutions. *Electrochim. Acta* **52**, 1169–1181 (2006).

43. R. Ding, I. P. Jones, In situ hydride formation in titanium during focused ion milling. *J. Electron Microsc.* **60**, 1–9 (2011).

44. H. Sawada, F. Hosokawa, A. I. Kirkland, Accurate evaluation of aberration for probe-forming system and influence of aberration on high-resolution STEM image. *J. Phys. Conf. Ser.* **902**, 012012 (2017).

45. Y. Kihn, C. Mirguet, L. Calmels, EELS studies of Ti-bearing materials and ab initio calculations. *J. Electron Spectrosc. Relat. Phenom.* **143**, 117–127 (2005).

46. R. Kilaas, Optimal and near-optimal filters in high-resolution electron microscopy. *J. Microsc.* **190**, 45–51 (1998).

47. K. Momma, F. Izumi, *VESTA* 3 for three-dimensional visualization of crystal, volumetric and morphology data. *J. Appl. Crystallogr.* **44**, 1272–1276 (2011).

48. J. Barthel, Dr. Probe: A software for high-resolution STEM image simulation. *Ultramicroscopy* **193**, 1–11 (2018).

49. L.-M. Peng, G. Ren, S. L. Dudarev, M. J. Whelan, Debye–Waller factors and absorptive scattering factors of elemental crystals. *Acta Crystallogr. A* **52**, 456–470 (1996).

50. A. Ishizuka, M. Oka, T. Seki, N. Shibata, K. Ishizuka, Boundary-artifact-free determination of potential distribution from differential phase contrast signals. *Microscopy* **66**, 397–405 (2017).

51. I. Lazić, E. G. T. Bosch, E. Yucelen, R. Imlau, L. Sorin, Thick (3D) sample imaging using iDPC-STEM at atomic scale. *Microsc. Microanal.* **24**, 170–171 (2018).

Citation: S. de Graaf, J. Momand, C. Mitterbauer, S. Lazar, B. J. Kooi, Resolving hydrogen atoms at metal-metal hydride interfaces. *Sci. Adv.* **6**, eaay4312 (2020).

Science Advances

Resolving hydrogen atoms at metal-metal hydride interfaces

Sytze de Graaf, Jamo Momand, Christoph Mitterbauer, Sorin Lazar and Bart J. Kooi

ARTICLE TOOLS	http://advances.sciencemag.org/content/6/5/eaay4312
SUPPLEMENTARY MATERIALS	http://advances.sciencemag.org/content/suppl/2020/01/27/6.5.eaay4312.DC1
REFERENCES	This article cites 48 articles, 0 of which you can access for free http://advances.sciencemag.org/content/6/5/eaay4312#BIBL
PERMISSIONS	http://www.sciencemag.org/help/reprints-and-permissions